Title

Ultrahigh-resolution scanning microwave impedance microscopy of moiré lattices and superstructures

Journal

Science Advances, 6(50)

ISSN

2375-2548

Authors

Lee, Kyunghoon
Utama, M Iqbal Bakti
Kahn, Salman
et al.

Publication Date

2020-12-11

DOI

10.1126/sciadv.abd1919

Peer reviewed

MATERIALS SCIENCE

Ultrahigh-resolution scanning microwave impedance microscopy of moiré lattices and superstructures

Kyunghoon Lee[1,2,3]*, M. Iqbal Bakti Utama[1,2,4]*, Salman Kahn[1,2]*, Appalakondaiah Samudrala[5], Nicolas Leconte[5], Birui Yang[1], Shuopei Wang[6,7], Kenji Watanabe[8], Takashi Taniguchi[9], M. Virginia P. Altoé[10], Guangyu Zhang[6,7], Alexander Weber-Bargioni[10], Michael Crommie[1,2,3], Paul D. Ashby[10], Jeil Jung[5], Feng Wang[1,2,3†], Alex Zettl[1,2,3†]

Two-dimensional heterostructures composed of layers with slightly different lattice vectors exhibit new periodic structure known as moiré lattices, which, in turn, can support novel correlated and topological phenomena. Moreover, moiré superstructures can emerge from multiple misaligned moiré lattices or inhomogeneous strain distributions, offering additional degrees of freedom in tailoring electronic structure. High-resolution imaging of the moiré lattices and superstructures is critical for understanding the emerging physics. Here, we report the imaging of moiré lattices and superstructures in graphene-based samples under ambient conditions using an ultrahigh-resolution implementation of scanning microwave impedance microscopy. Although the probe tip has a gross radius of ~100 nm, spatial resolution better than 5 nm is achieved, which allows direct visualization of the structural details in moiré lattices and the composite super-moiré. We also demonstrate artificial synthesis of novel superstructures, including the Kagome moiré arising from the interplay between different layers.

INTRODUCTION

Moiré lattices with large periodicity can be realized in two-dimensional (2D) heterostructures composed of atomically thin layers with slightly different lattice vectors, either due to a lattice mismatch or a small-angle twist. Such moiré lattices generate a new length and energy scale in stacked 2D materials and provide an exciting new platform to engineer novel correlated phenomena and topological physics in van der Waals heterostructures (*1*–*12*). Superstructures of moiré lattices can emerge if multiple layers with similar lattice vectors are stacked together, offering extra flexibility to design novel quantum phenomena.

Quantitative characterization of the moiré lattice and superstructure in a device configuration is critical for understanding and controlling the rich moiré physics in 2D heterostructures. Traditionally, the structure of moiré lattices is imaged with transmission electron microscopy (TEM) (*13*, *14*) and scanning tunneling microscopy (STM) (*15*–*20*), but these methods have low throughput and require specialized sample preparation that is largely unsuitable for functional devices. Different imaging modalities based on atomic force microscopy (AFM) have also been explored to study moiré lattices (*21*–*26*), but imaging moiré lattices and superstructures with sufficient sensitivity and resolution is challenging.

Relative to other AFM- and TEM-based techniques, scanning microwave impedance microscopy (sMIM) (*27*) is an attractive moiré imaging tool because, in principle, it combines the benefit of reasonable spatial resolution, high sensitivity to local electrical properties, and compatibility with functional electronic devices. Here, we demonstrate an ultrahigh-resolution implementation of sMIM, which we term uMIM, with which we perform nanoscale imaging of moiré lattices and superstructures in various graphene-based devices under ambient conditions. We show that a spatial resolution better than 5 nm can be achieved with uMIM despite the gross scanning probe tip radius being ~100 nm. Owing to the strong sensitivity of the uMIM signal on the local conductivity of the sample, uMIM can probe not only the regular moiré lattice in twisted graphene and graphene/hBN (hexagonal boron nitride) heterostructures but also the moiré superstructures formed by multiple stacked layers. We use uMIM imaging to reveal several moiré superstructures, including a supermodulation of the moiré lattice and a novel Kagome-like moiré structure that arises from the interplay between closely aligned twisted graphene and hBN layers. Such moiré superstructures can offer new avenues to engineer quantum phenomena in van der Waals heterostructures.

RESULTS

A highly simplified schematic for our measurements is illustrated in Fig. 1A. sMIM probes the local complex tip-sample admittance, and the signals are represented by the real and imaginary responses (*27*). The tip-sample admittance depends sensitively on the local sample conductivity. Figure 1B shows the calculated real and imaginary uMIM signals, uMIM-Re and uMIM-Im, as functions of the sample sheet conductance (g), using the inferred ultrahigh-resolution modified tip geometry (see Materials and Methods and the Supplementary Materials). We note that the uMIM-Im signal is informative for a rapid assessment of the local conductivity because it increases monotonically with g. Simulated sMIM-Re and sMIM-Im for the gross (unmodified) tip geometry [scanning electron microscopy (SEM) image of Fig. 1A] are presented in fig. S14A.

[1]Department of Physics, University of California at Berkeley, Berkeley, CA 94720, USA. [2]Materials Sciences Division, Lawrence Berkeley National Laboratory, Berkeley, CA 94720, USA. [3]Kavli Energy NanoSciences Institute at the University of California, Berkeley and the Lawrence Berkeley National Laboratory, Berkeley, CA 94720, USA. [4]Department of Materials Science and Engineering, University of California at Berkeley, Berkeley, CA 94720, USA. [5]Department of Physics, University of Seoul, Seoul, South Korea. [6]Beijing National Laboratory for Condensed Matter Physics and Institute of Physics, Chinese Academy of Sciences, Beijing 100190, China. [7]Collaborative Innovation Center of Quantum Matter, Beijing, China. [8]Research Center for Functional Materials, National Institute for Materials Science, 1-1 Namiki, Tsukuba 305-0044, Japan. [9]International Center for Materials Nanoarchitectonics, National Institute for Materials Science, 1-1 Namiki, Tsukuba 305-0044, Japan. [10]Molecular Foundry, Lawrence Berkeley National Laboratory, Berkeley, CA 94720, USA.
*These authors contributed equally to this work.
†Corresponding author. Email: azettl@berkeley.edu (A.Z.); fengwang76@berkeley.edu (F.W.)

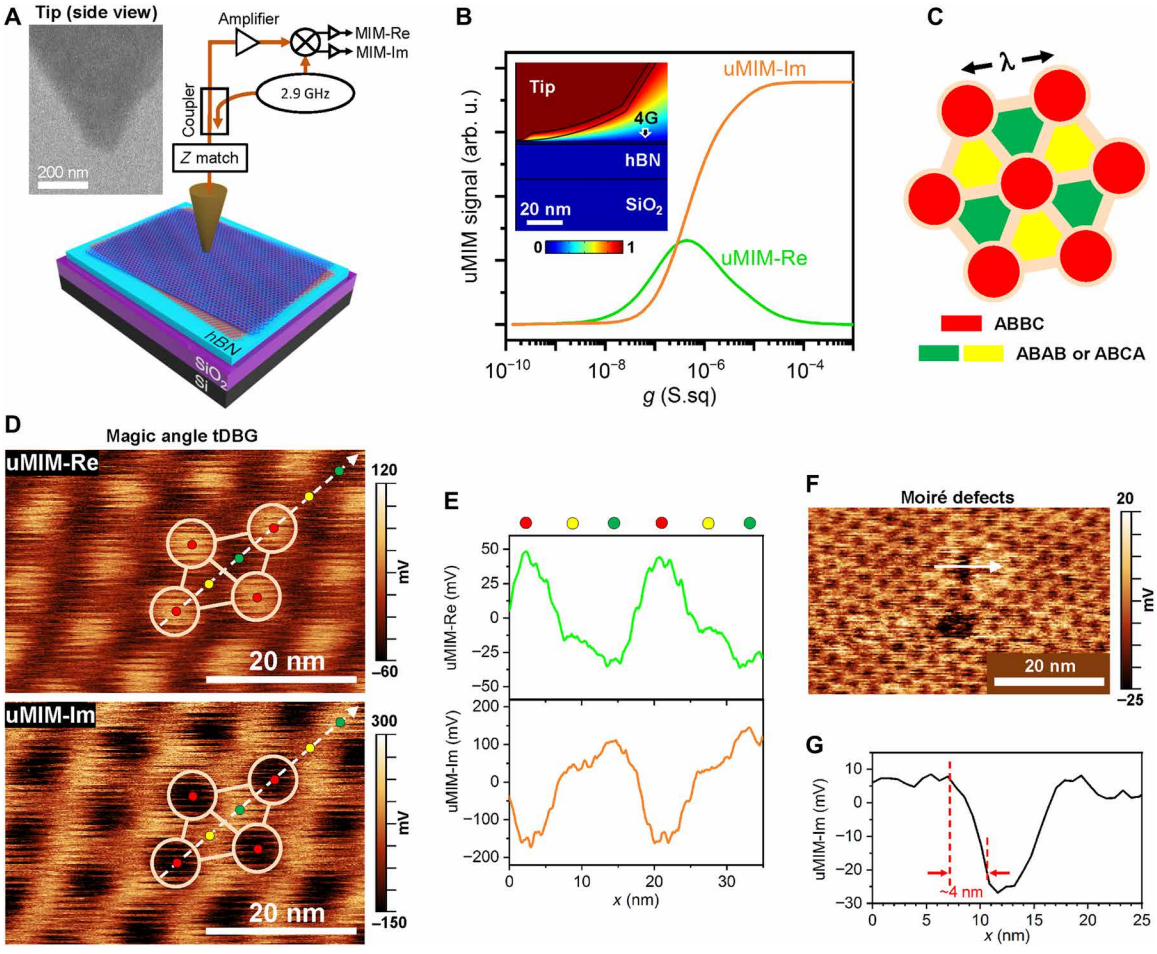

Fig. 1. Imaging mechanism and spatial resolution of uMIM. (**A**) Measurement configuration. Inset: Gross SEM image of the tip. (**B**) Calculated uMIM signals as a function of the sample sheet resistance, assuming modified tip (see the Supplementary Materials). Inset: Simulated quasi-static potential due to tip-sample interaction. Only half of the tip is shown. arb. u., arbitrary unit. (**C**) Moiré lattice in a tDBG. λ denotes the moiré period. Red circles mark the ABBC stacking, while green and yellow indicate either ABAB or ABCA. (**D**) uMIM images of the moiré lattice in a tDBG with the magic angle twist of ~1.3°. The stacking boundaries are superimposed onto the images, with the dots indicating the stacking following the color code in (A). (**E**) uMIM signal profiles along the white dashed arrows in (D), averaged over 20 pixels width. The locations of different stacking are marked by colored dots. (**F**) A uMIM-Im image on a tDBG with isolated moiré defects. (**G**) The signal profile along the white arrow in (F).

sMIM can be considered a microwave version of the apertureless near-field optical microscopy. However, unlike typical near field microscopy, our experiments are performed in contact mode where the tip-sample distance is maintained in the repulsive regime. Consequently, the electromagnetic coupling between the tip and sample is highly localized at the tip apex. Previous studies have demonstrated that the resolution of sMIM and other near-field techniques is limited by tip geometry, with the tip radius setting the resolution limit (typically 50 to 100 nm). To achieve ultrahigh resolution, we use a conventional sMIM instrument in air at room temperature, but specially prepare (i.e., condition) the tip and sample. Briefly, using the same tip throughout, the sample is first prescanned over a large area. A detailed small-area data-collecting scan is then performed. We hypothesize that the conditioning step results in (i) sample surface cleaning and (ii) tip geometry modification. Regarding the latter, both electrically conducting and insulating adsorbates from the sample redistribute onto the tip apex, eventually forming a protruding thin conducting chain supported by an insulating matrix. This results in an electromagnetic coupling that is dominated by the metallic chain, while the signal contribution from the remaining part of the bulk recessed tip is suppressed. This scenario, somewhat akin to the enhanced resolution afforded to STM-AFM by tip-adsorbed CO molecules (*28*, *29*) and to conductive AFM by the formation of metallic filament near tip apex (*30*, *31*), facilitates spatial resolution significantly finer than the gross radius of the tip. Direct evidence of such tip modification after scanning is shown in figs. S2 (SEM) and S3 (TEM) (see also Materials and Methods and fig. S15 for further illustrations and discussion) (*32*).

We first demonstrate the capability of uMIM by imaging the moiré superlattice in twisted double bilayer graphene (tDBG). Similar to twisted bilayer graphene (tBG) (*2*), tDBG contains a continuously varying stacking sequence within the moiré unit cell (*6*). The tDBG unit cell contains one truncated triangular domain each of ABAB (Bernal) and ABCA (rhombohedral) stacking, with a nearly circular ABBC stacking at the vertices of each triangle (Fig. 1C). Figure 1D shows a uMIM map of a tDBG sample, where we resolve the moiré period from the contrasts of signal arising from the different local stacking. The measured moiré period of this sample is (10.9 ± 0.7) nm,

corresponding to a twist angle of θ= (1.3 ± 0.1)°, the "magic angle" in tDBG for which field-tunable correlated insulating and superconducting states have been reported (*7*–*10*).

We resolve three different domains in the tDBG moiré lattice with distinct uMIM signals (Fig. 1, D and E). Our result demonstrates the usefulness of uMIM in identifying fine structures of moiré lattices in 2D heterostructures based on the local conductivity. We assign the domains with the weakest uMIM-Im signal (i.e., the smallest local conductivity) as the ABBC stacking. Analogous to the circular AA stacking in tBG (*17*), the circular ABBC domains in tDBG occupy a proportion of the moiré unit cell that is relatively larger than the other two stacking domains. However, because of the lattice relaxation with decreasing twist angle at θ< 1°, the proportion of ABBC domain in the moiré unit cell continually decreases up until it disappears for near-0° twist, leaving only triangular ABAB-ABCA domains (e.g., Fig. 2C). Consistent with this trend, we observe the decrease in the size proportion in domains with the weakest uMIM-Im signal in tDBG with twist angle of 0.6° (fig. S5). Meanwhile, the two different contrasts in regions between ABBC stacking are attributed to the ABCA and ABAB domains.

The spatial resolution capability of uMIM is further demonstrated in the imaging of "moiré defects," which interrupt the long-range periodicity of the moiré lattice. In Fig. 1 (F and G) (and fig. S6), we can readily resolve the moiré defects with sub–5-nm resolution, outperforming other optical near-field microscopes. The topography images around the moiré defects were provided in fig. S6 (A to C), which do not show any special feature around the moiré defect beyond the *z* resolution of the AFM (less than ~40 pm root-mean-square noise level). This suggests that the apparent moiré defect does not arise from residual contamination that are trapped between the layers, as such contaminants tend to form large bubbles with thickness and size between 10 and 500 nm (*33*). We also do not expect that the moiré defects are caused by tip damage because we typically use a relatively gentle tip-sample contact force of ~1 to 5 nN, and we did not see any emergence of sample damage after multiple scans of the same area over 5 hours (see fig. S8). The observed moiré defect is analogous in appearance to the point defects that interrupt the long-range periodicity in the atomic lattice. Similar point defect-like structure in moiré lattice was also previously observed in other graphitic systems by STM imaging (*34*–*36*). For graphene-based moiré lattices that are homogenous with van der Waals interactions primarily bonding the layers, we should view the point defects in the moiré lattice as a local change of the atomic registry between the graphene and hBN atoms, which thus affect the stacking order.

Figure 2 demonstrates the universal applicability of uMIM in resolving moiré structures in various graphene-based systems. Particularly, uMIM can visualize the inhomogeneity and defect structures in the moiré lattices (also see fig. S9). Figure 2A shows the moiré observed in epitaxially grown monolayer graphene/hBN. The sample was synthesized using a standard plasma-enhanced chemical vapor deposition (CVD) at elevated temperature (*37*). Such aligned graphene/hBN system exhibits a transition into a commensurate moiré stacking (*21*), where the graphene lattice expands to accommodate the mismatch with hBN. This results in a hexagonal domain-wall network (thin bright lines in Fig. 2A) with accumulated strain, as has been substantiated from the Young's modulus mapping and the lattice constant measurement by STM in (*21*). The moiré period from fast Fourier transform (FFT; Fig. 2A, inset) is determined to

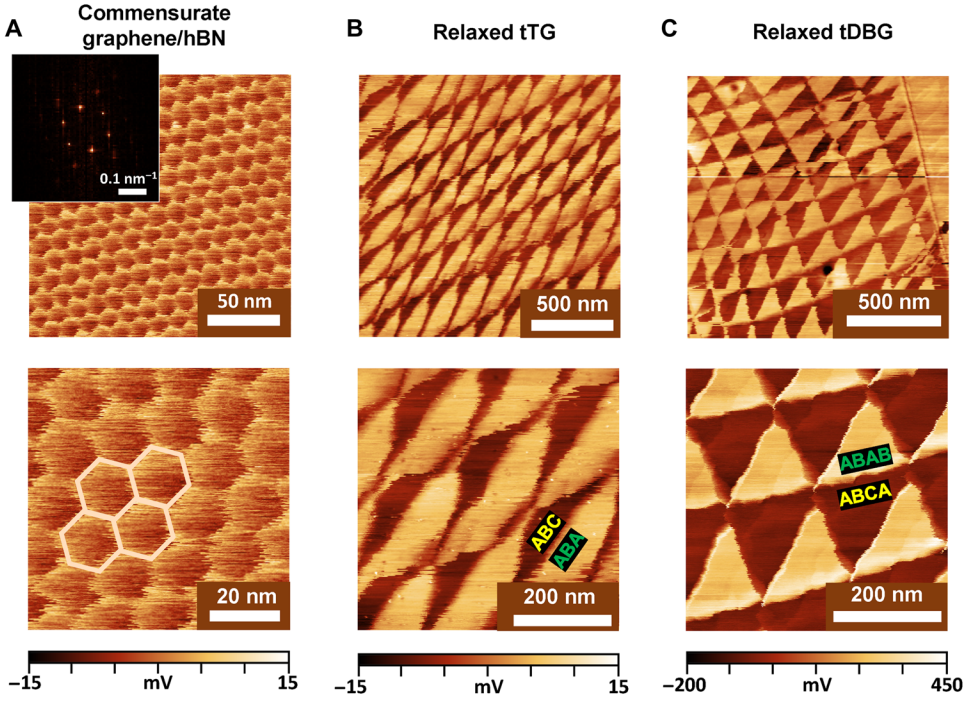

Fig. 2. Versatility of uMIM in imaging various graphene-based moiré lattices. The lower row shows detailed uMIM-Im scans from each corresponding frame in the upper row. (**A**) Commensurate, epitaxial monolayer graphene/hBN. The FFT of (A) is shown as the inset. In the lower row, beige hexagons are superimposed to the thin domain walls that result from the commensurate transition in the graphene/hBN sample. (**B**) Near-0° tTG with relaxed ABA and ABC domains. (**C**) Near-0° tDBG with relaxed ABAB and ABCA domains. The upper row shows the large area scans of uMIM-Im signal.

be (16.1 ± 0.5) nm, close to that expected for perfectly aligned graphene and hBN layers.

At near-0° twist, the lattice energetically prefers to reconstruct into relaxed triangular domains with an alternating stacking sequence (*14*, *38*, *39*). In twisted trilayer graphene (tTG) and tetralayer tDBG, these domains correspond to Bernal (ABA and ABAB) and rhombohedral stacking (ABC and ABCA), respectively. Each stacking order results in different low-energy electronic band structure (*40*). The rhombohedral stacking in few-layer graphene owns flat bands with bandwidth that scales inversely with the layer number (*40*), making it an attractive platform to study correlation physics (*5*, *6*, *11*, *12*). With the rarity of rhombohedral stacks from their relative instability, the near-0° twist presents an alternative route for generating the stacking (*6*).

The low Fermi velocity in rhombohedral stacking as compared with Bernal stacking should result in a lower electrical conductivity for the rhombohedral domain. In Fig. 2 (B and C), the triangular domains in tTG and tDBG are successfully resolved owing to this local conductivity variation, where the domains with lower uMIM-Im signal are assigned to the rhombohedral stack (ABC in tTG, ABCA in tDBG). In addition, Fig. 2B also shows possible strain effects at the domain walls and vortices, leading to a deviation of the domain shape from regular triangle.

In addition to the conventional moiré lattices, our ultrahigh-sensitivity uMIM allows for imaging of moiré superstructures from three underlying lattices with different lattice vectors. Although heterostructures with multiple coexisting moiré have been imaged before with AFM (*25*), the resulting moiré superstucture has not been observed in ambient conditions previously. Figure 3 (A to C) shows a twisted double bilayer graphene on hBN (BG/BG/hBN) heterostructure where the two BGs are slightly twisted and the bottom BG is nearly aligned with the underlying hBN flake. Two moiré lattices are present: one from the tDBG and the other from the aligned BG/hBN. They can interfere and form a supermodulation pattern with very large periodicity. Figure 3A shows such moiré superstructure. The FFT pattern reveals three distinct periods (Fig. 3B). Two sets of the moiré periods (red and blue dashed hexagons) have similar periodicity of (14.1 ± 0.4) nm and (12.3 ± 0.7) nm, and we identify them as the underlying moiré lattices between BG/BG and BG/hBN (i.e., $\lambda_{BG/BG}$ and $\lambda_{BG/hBN}$, respectively). The other set of spots in FFT (purple dashed hexagon) has a much longer period of 45.7 nm, which we ascribe to the supermodulation of the moirés. Such a periodicity cannot be assigned to BG/hBN moiré as it requires too large a strain in the graphene lattice, nor to BG/BG moiré, as at this length scale the moiré should relax into triangular domains (*14*). As a check, we compare this periodicity with the expected period of a super-moiré from the two constituent moirés (*41*)

$$\lambda_s = \frac{1}{\sqrt{\left(\frac{1}{\lambda_{BG/BG}}\right)^2 + \left(\frac{1}{\lambda_{BG/hBN}}\right)^2 - \frac{2\cos(\Delta\theta_s)}{\lambda_{BG/BG}\lambda_{BG/hBN}}}} \quad (1)$$

where $\Delta\theta_s = 14.7°$ is the misorientation between the moirés. This results in λ_s of ~45.2 nm, which agrees well with the observed periodicity of 45.7 nm. Figure 3C shows the real-space image for each moiré as filtered from the first-order spots in the FFT. The other faint spots in Fig. 3B are the higher-order FFT spots from the moiré lattices and the resulting superstructures. The reciprocal vector that describes these higher-order spots can be given as a linear combination of the vectors from the first-order spots (the labeling is shown in fig. S12). However, the first-order spots are already sufficient in determining the moiré periodicities.

A different moiré superstructure can exist when a near-0° tDBG with triangular relaxed domains are intertwined with the commensurate moiré from aligned bottom BG/hBN (Fig. 3D). This combination results in an apparent reconstruction of the BG/hBN moiré near the ABAB-ABCA domain walls. An indication of this is seen in the FFT (Fig. 3E), where the pattern corresponding to the BG/hBN moiré (dashed blue square) no longer appears as single isolated spots. Filtering the uMIM-Im image by selecting only these features (Fig. 3F) clarifies the supermodulation of BG/hBN moiré occurring near the domain wall. We believe that this feature is not an artifact, as similar behavior can be seen in a smaller area uMIM-Im scan (Fig. 3F) and from the topographic image (fig. S13). Such modification of the moiré structure might lead to a modified electronic spectrum, which may need to be incorporated in theoretical calculations of the electronic structure.

uMIM imaging allows us to readily explore other moiré superstructures with desirable physical properties. A special example is the Kagome lattice, which has attracted notable attention as a platform to study Hubbard physics because of the presence of flat bands and exotic quantum and magnetic phases with nontrivial ordering (*42*–*44*). However, crystals with a natural Kagome lattice are relatively rare. In ultracold atom research, a Kagome lattice can be simulated via an optical superlattice. For example, one type of such a corner-sharing triangular superlattice, called the trimerized Kagome lattice, can be constructed by superimposing two triangular optical lattices with 2:1 periodicity (*45*, *46*).

Inspired by the artificial Kagome lattice in optical superlattices, we construct a solid-state Kagome-like moiré superlattice in BG/BG/hBN systems by superimposing $\lambda_{BG/BG} : \lambda_{BG/hBN} = 2:1$ and maintaining azimuthal alignment of the moiré constituents. These are achieved by setting the twist angle of both the BG/BG and BG/hBN interfaces to $\theta \approx 0.6°$ (Fig. 4, A and B). We visualize such a special moiré composite with uMIM (Fig. 4C) and confirm from FFT the presence of two aligned moirés with periods of $\lambda_{BG/BG} = (24.5 \pm 1.1)$ nm and $\lambda_{BG/hBN} = (13.1 \pm 0.1)$ nm. The resulting structure is examined in more detail in Fig. 4F and compared with the expected structure for an ideal Kagome lattice (Fig. 4G).

The construction of a solid-state Kagome-like lattice based on moiré patterns is an interesting pathway to explore the possibility of generating nearly flat bands and host correlated phases in the vicinity of the Fermi level. While the superlattice miniband structures are susceptible to changes in the details of the atomic and electronic structure models, the band flatness should further be enhanced since the BG within the tDBG has less dispersive bands than a Dirac cone at the K points, and since a gap can open through interaction with the substrate. Figure 4H shows the calculated band structure around the Fermi level of the Kagome-like moiré (see the Supplementary Materials for calculation details). A series of minibands with small bandwidth are observed, including flat conduction bands with a bandwidth of ~3 meV.

DISCUSSION

We have demonstrated ultrahigh-resolution uMIM as a facile, high-throughput, and noninvasive method for characterizing moiré lattices and superstructures, as well as moiré defects and the creation

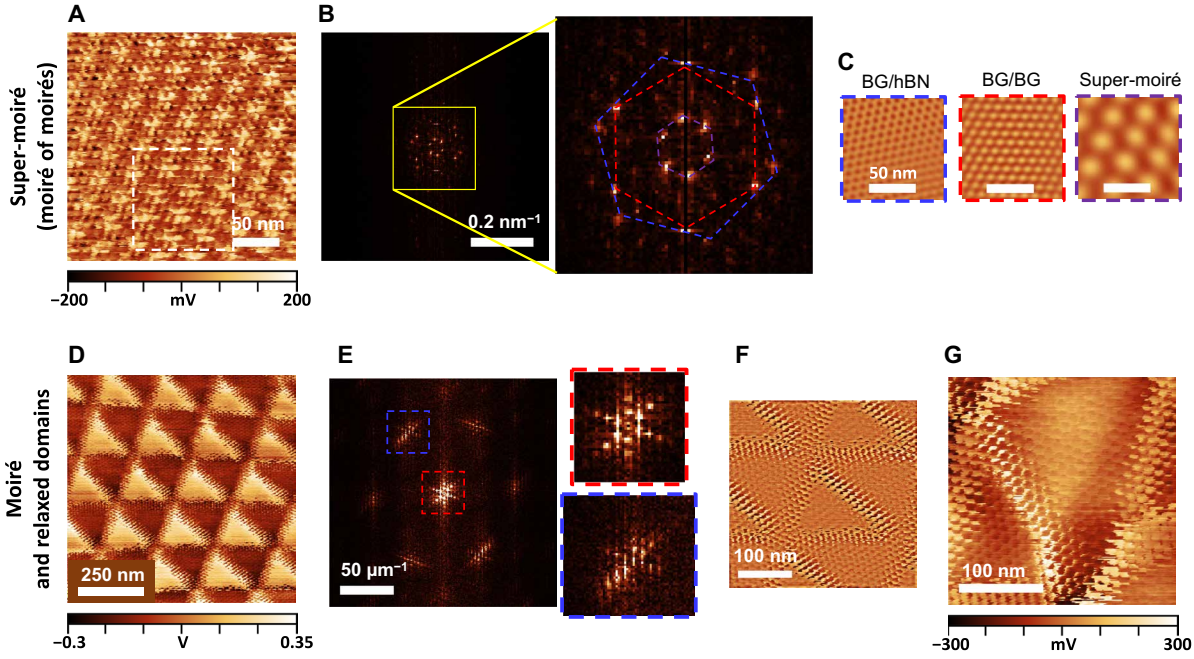

Fig. 3. Superstructures from tDBG and hBN moirés. (**A** to **C**) Super-moiré lattice: a moiré-of-moirés. (A) uMIM-Im image. (B) The FFT image of (A). The dashed hexagons marked the first-order period of lower BG/hBN moiré (blue), BG/BG moiré (red), and the emerging super-moiré (purple). (C) Fourier-filtered image of the area inside the white dashed square in (A) based on the first-order moiré spots. (**D** to **G**) The composite of triangular ABAB-ABCA domains in near-0° tDBG with BG/hBN moiré. (D) uMIM-Im image. The BG/hBN moiré appears enhanced near the domain borders. (E) The FFT image of (D). The insets show the feature corresponding to the BG/hBN moiré (blue border) and triangular network (red border). (F) Fourier-filtered image of the features corresponding to the BG/hBN moiré. (G) Detailed image of a triangular domain.

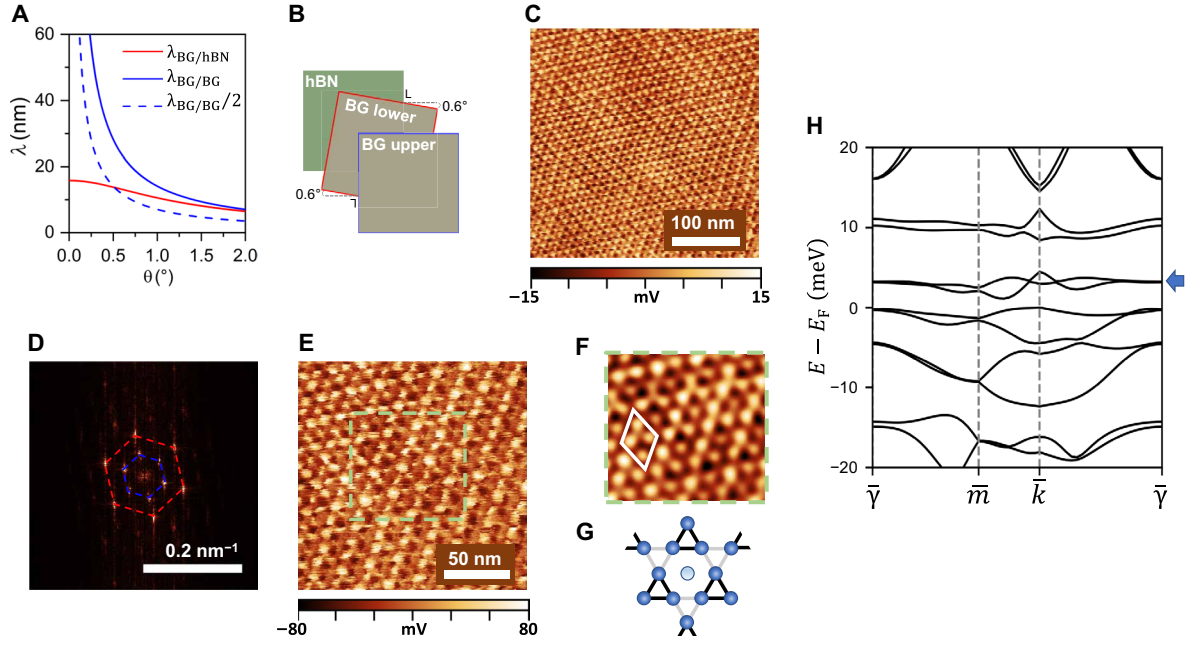

Fig. 4. Kagome-like moiré superstructure in tDBG/hBN. (**A**) Calculated moiré period of BG/BG and BG/hBN stacks as a function of twist angle. The condition $\lambda_{BG/BG}/\lambda_{BG/hBN} = 2$ is achieved at $\theta \approx 0.6°$. (**B**) The sample scheme to realize Kagome-like moiré. The BG/hBN and BG/BG flakes are twisted by 0.6°, but the hBN and the upper BG are aligned. (**C**) uMIM-Im image. (**D**) FFT of the image in (C). The dashed hexagons mark the first-order spots of BG/hBN moiré (red) and BG/BG moiré (blue). (**E**) Detailed uMIM-Im scan of Kagome-like moiré. (**F**) Low-pass filtered image from the area inside the green square in (E). The unit cell of the Kagome-like moiré is marked with a white diamond. (**G**) An illustration of a trimerized Kagome lattice resembling the observed moiré. (**H**) Calculated band structure of the Kagome-like moiré lattice. The high symmetry points refer to that of the Brillouin zone of the BG/BG/hBN superstructure. The blue arrow marks the flat bands near the Fermi level.

of tailored Kagome superlattices in multilayer stacks of graphene-based van der Waals heterostructures. The enhanced capability enabled by uMIM should facilitate better understanding and heterostructure design paths for novel correlated quantum phenomena in more advanced moiré superstructures. Recent sMIM studies showed a measurement of electronic ground states of the moiré system at partial fillings at low temperature (*47*, *48*), and it will be interesting to probe such states with high spatial resolution via uMIM.

We believe that uMIM should be applicable to other 2D moiré systems as well. Since the sample needs to be sufficiently conducting for a good signal-to-noise ratio, moiré imaging with uMIM should work well in other metallic and semimetallic 2D materials, such as WTe_2 or $NbSe_2$. For these systems, uMIM holds a great advantage as a facile method that does not require any special sample preparation nor processing steps, such as the need for electrical contact as required in STM or conducting AFM. For insulating or semiconducting 2D materials, the moiré lattice can be imaged if the sample is modified to be sufficiently conducting. For example, this can be achieved by doping via atomic substitution, by surface adsorbates of dopant species, or by electrostatic gating. The gating approach can be most preferable with its in situ tunability, although it requires wiring process for electrical grounding and application of external gate bias to modulate the carrier density.

MATERIALS AND METHODS

Sample fabrication

For monolayer graphene on hBN, the sample was grown via plasma-assisted CVD method following (*37*). For other samples, we followed either (i) the "flip-chip" procedure with polypropylene carbonate stamp as described in (*2*) or (ii) the transfer procedure with polycarbonate stamp as described in (*18*). In both cases, we have used the tear-and-stack step (*49*, *50*) for twist angle control. tTG was made by stacking a monolayer and a bilayer segment of the same flake. tDBG was made by stacking a bilayer and another bilayer segment of the same flake. All graphene-based samples were sitting on a thin (10 to 30 nm) hBN flake to ensure topography flatness. The van der Waals heterostructure stacks are placed on a highly doped Si substrate with 285-nm oxide film, as shown in Fig. 1A.

Ultrahigh-resolution scannning microwave impedance microscopy

The uMIM imaging was performed with Asylum MFP-3D AFM with commercial ScanWave electronics and shielded cantilever (PrimeNano Inc.) (*27*, *51*). Microwave frequency of 2.9 to 3.0 GHz was used in the measurement. Low-power (0.3 to 3 μW) microwave excitation is delivered to the metallic tip through the impedance matching circuit, and the reflected signal is collected with being amplified and demodulated to give the images of the real (resistive) and imaginary (capacitive) parts of tip-sample complex admittance. All topography and uMIM images were collected concurrently in contact mode under ambient condition. The tip-sample distance was maintained in the repulsive regime, with the Pauli repulsion of the electron density of the outermost atoms of the tip and sample providing the repulsive force. As a critical step to achieve ultrahigh resolution, before data collection imaging, the tip is scanned multiple times over a relatively large sample area to clean the sample surface and to improve the uMIM signal from the moiré lattice. Consequently, imaging with sub–5-nm spatial resolution can be performed (Fig. 1G and figs. S6 and S7), which is superior to previous sMIM reports (*32*, *52*–*59*).

Tip modification for uMIM imaging

We find that the large-area prescan conditioning is essential to achieve the ultrahigh resolution for uMIM. The prescan serves two purposes. (i) The sample is swept of unwanted debris and chemical contaminants, and (ii) the tip is modified. Previous sMIM experimental and modeling studies have demonstrated that the achievable spatial resolution is of the order of the tip radius. Hence, with a conventional metallic tip apex having a radius of curvature of ~50 to 100 nm, sMIM near-field imaging is limited to 50 to 100 nm.

uMIM achieves <5-nm resolution via a proposed tip modification mechanism somewhat akin to the marked AFM resolution enhancement afforded by attaching a CO molecule to the AFM tip (*28*, *29*). During our prescanning conditioning process, adsorbate contaminations from the sample surface are attached to the tip, creating a thin dielectric slab on the tip apex. A uniform but thin dielectric coating on the tip will result in a weakened electromagnetic coupling between the tip and sample, but will not appreciably enhance resolution. However, along with dielectric contaminants, the tip also picks up metallic species (these can also originate from the tip itself). The metallic species can form conducting chains through the dielectric, essentially creating a secondary, ultrasharp tip protruding from the first, essentially through a window in the dielectric. This secondary atomically fine tip is mechanically stabilized by the rigid surrounding dielectric medium. In fig. S3, we provide direct evidence for such tip modification via TEM bright-field and high-angle annular dark-field imaging, along with energy-dispersive x-ray analysis. We further corroborate the imaging enhancement provided by such a modification by simulating the electric field distribution around the tip-sample interface in fig. S15 for the two scenarios of tip geometry: unmodified tip (fig. S15A) and tip modified with dielectric and conducting chain (fig. S15C). The field enhancement from the modified tip (fig. S15F) is significantly more localized under the tip apex, facilitating improvements in the spatial resolution in the imaging as compared with that from the original clean metallic tip (fig. S15D) or from the tip without the metallic protrusion in the dielectric coating. We note that resolution enhancement via formation of conducting wire near the tip apex has also been reported before in conductive AFM mode (*30*).

Consistent with our finding, previous sMIM work has shown that, occasionally, obvious tip blunting in contact mode imaging is not always deleterious to spatial resolution (*32*). In that work, point asperities induced during the "blunting" process similar to the metallic chains proposed here could be the source of the "maintained" resolution. We have observed similar effects for blunted tips in uMIM (fig. S2, C and D). In the case of sMIM imaging with a clean unmodified metallic tip, the large area tip-sample contact is the limiting factor for resolution.

Simulation of the tip-sample interaction

All simulations were performed with finite element analysis using the commercial COMSOL 5.2 software. For the simulation in Fig. 1C and fig. S9, we follow the method described in (*55*). The sMIM and uMIM signals are considered to be directly proportional to the complex tip-sample admittance contrasts (fig. S14, A and B). The tip geometry for "unmodified" tips is determined from scanning electron microscopy (Fig. 1A). A finite distance of 0.5 nm was used

between the sample and the metallic tip apex (both the unmodified and modified geometry) in Fig. 1B and fig. S14 (A and B). Simulations for the modified tip assumed the parameters of dielectric thickness (4 nm), dielectric coating (ε_r: 2.5), and base width of the metallic protrusion (20 nm). While varying the sample-tip distance influences the magnitude of the admittance contrast (fig. S13D), the relative shape and ratio between the MIM-Im and MIM-Re curves are only weakly dependent on the tip-sample distance (fig. S13E).

For fig. S15, the simulated electric field enhancement is made with an unpolarized incoming electromagnetic wave traveling in the y direction. The graphene layer is modeled with a field-dependent surface current density atop the hBN layer. For the simulation, we used a tip-sample distance of 2.5 nm.

Band structure calculation

We performed the band structure calculation using a tight-binding model informed from ab initio density functional theory (DFT) calculations for the atomic and electronic structures. The atomic structure includes the relaxation effects through LAMMPS (Large-scale Atomic/Molecular Massively Parallel Simulator) molecular dynamic simulations (*60*) using force fields parameterized to fit the random phase approximation total energy data (EXX + RPA) for different local stacking configurations of BG (*61*–*63*). Our Kagome-like moiré is built from a superposition of two moiré patterns, one from the BG/BG interface and another from BG/hBN, which are commensurately superposed and whose bands can be folded into a small superstructure Brillouin zone. A commensurate moiré superlattice is generated with ~0.6° in twist angle of the tDBG. As a first step, we have relaxed the tDBG system (containing 71,288 atoms) using LAMMPS, leading to a first moiré pattern. The Kagome-like moiré superstructure is generated by superimposing the effective tight binding model between hBN and the bottom graphene layer of tDBG. For the effective moiré pattern model in tDBG/hBN, we have considered ~1.8% lattice mismatch and ~0.6° twist angle between tDBG and hBN. The hopping parameters in the BG parts of tDBG uses the F2G2 model (*64*) with the intralayer hopping terms tuned to give an effective nearest-neighbor hopping term of $t_0 = -3.1$ eV with a Fermi velocity of $v_F = 1.05 \times 10^6$ m/s. The intersurface hopping terms between the twisted surfaces of graphene are modeled from parameters stemming from DFT calculations (*65*, *66*) and through effective moiré potentials on the bottom layer graphene for the interface between graphene and hBN (fig. S15) (*64*, *67*, *68*). As a comparison, fig. S16 shows the calculated band structure for only the bottom BG/hBN and for the tDBG without hBN substrate.

SUPPLEMENTARY MATERIALS

Supplementary material for this article is available at http://advances.sciencemag.org/cgi/content/full/6/50/eabd1919/DC1

REFERENCES AND NOTES

1. R. Bistritzer, A. H. MacDonald, Moiré bands in twisted double-layer graphene. *Proc. Natl. Acad. Sci. U.S.A.* **108**, 12233–12237 (2011).
2. M. I. B. Utama, R. J. Koch, K. Lee, N. Leconte, H. Li, S. Zhao, L. Jiang, J. Zhu, K. Watanabe, T. Taniguchi, P. D. Ashby, A. Weber-Bargioni, A. Zettl, C. Jozwiak, J. Jung, E. Rotenberg, A. Bostwick, F. Wang, Visualization of the flat electronic band in twisted bilayer graphene near the magic angle twist. *Nat. Phys.* 10.1038/s41567-41020-40974-x, (2020).
3. S. Lisi, X. Lu, T. Benschop, T. A. de Jong, P. Stepanov, J. R. Duran, F. Margot, I. Cucchi, E. Cappelli, A. Hunter, A. Tamai, V. Kandyba, A. Giampietri, A. Barinov, J. Jobst, V. Stalman, M. Leeuwenhoek, K. Watanabe, T. Taniguchi, L. Rademaker, S. J. van der Molen, M. Allan, D. K. Efetov, F. Baumberger, *Direct Evidence for Flat Bands in Twisted Bilayer Graphene from Nano-Arpes* (2020); https://arxiv.org/abs/2002.02289.
4. Y. Cao, V. Fatemi, A. Demir, S. Fang, S. L. Tomarken, J. Y. Luo, J. D. Sanchez-Yamagishi, K. Watanabe, T. Taniguchi, E. Kaxiras, R. C. Ashoori, P. Jarillo-Herrero, Correlated insulator behaviour at half-filling in magic-angle graphene superlattices. *Nature* **556**, 80–84 (2018).
5. G. Chen, L. Jiang, S. Wu, B. Lyu, H. Li, B. L. Chittari, K. Watanabe, T. Taniguchi, Z. Shi, J. Jung, Y. Zhang, F. Wang, Evidence of a gate-tunable Mott insulator in a trilayer graphene moiré superlattice. *Nat. Phys.* **15**, 237–241 (2019).
6. A. Kerelsky, C. Rubio-Verdú, L. Xian, D. M. Kennes, D. Halbertal, N. Finney, L. Song, S. Turkel, L. Wang, K. Watanabe, T. Taniguchi, J. Hone, C. Dean, D. Basov, A. Rubio, A. N. Pasupathy, *Moiré-Less Correlations in ABCA Graphene* (2019); https://arxiv.org/abs/1911.00007.
7. G. W. Burg, J. Zhu, T. Taniguchi, K. Watanabe, A. H. MacDonald, E. Tutuc, Correlated insulating states in twisted double bilayer graphene. *Phys. Rev. Lett.* **123**, 197702 (2019).
8. X. Liu, Z. Hao, E. Khalaf, J. Y. Lee, Y. Ronen, H. Yoo, D. H. Najafabadi, K. Watanabe, T. Taniguchi, A. Vishwanath, P. Kim, Tunable spin-polarized correlated states in twisted double bilayer graphene. *Nature* **583**, 221–225 (2020).
9. Y. Cao, D. Rodan-Legrain, O. Rubies-Bigorda, J. M. Park, K. Watanabe, T. Taniguchi, P. Jarillo-Herrero, Tunable correlated states and spin-polarized phases in twisted bilayer–bilayer graphene. *Nature* **583**, 215–220 (2020).
10. C. Shen, Y. Chu, Q. Wu, N. Li, S. Wang, Y. Zhao, J. Tang, J. Liu, J. Tian, K. Watanabe, T. Taniguchi, R. Yang, Z. Y. Meng, D. Shi, O. V. Yazyev, G. Zhang, Correlated states in twisted double bilayer graphene. *Nat. Phys.* **16**, 520–525 (2020).
11. G. Chen, A. L. Sharpe, P. Gallagher, I. T. Rosen, E. J. Fox, L. Jiang, B. Lyu, H. Li, K. Watanabe, T. Taniguchi, J. Jung, Z. Shi, D. Goldhaber-Gordon, Y. Zhang, F. Wang, Signatures of tunable superconductivity in a trilayer graphene moiré superlattice. *Nature* **572**, 215–219 (2019).
12. G. Chen, A. L. Sharpe, E. J. Fox, Y.-H. Zhang, S. Wang, L. Jiang, B. Lyu, H. Li, K. Watanabe, T. Taniguchi, Z. Shi, T. Senthil, D. Goldhaber-Gordon, Y. Zhang, F. Wang, Tunable correlated Chern insulator and ferromagnetism in a moiré superlattice. *Nature* **579**, 56–61 (2020).
13. J. S. Alden, A. W. Tsen, P. Y. Huang, R. Hovden, L. Brown, J. Park, D. A. Muller, P. L. McEuen, Strain solitons and topological defects in bilayer graphene. *Proc. Natl. Acad. Sci. U.S.A.* **110**, 11256–11260 (2013).
14. H. Yoo, R. Engelke, S. Carr, S. Fang, K. Zhang, P. Cazeaux, S. H. Sung, R. Hovden, A. W. Tsen, T. Taniguchi, K. Watanabe, G.-C. Yi, M. Kim, M. Luskin, E. B. Tadmor, E. Kaxiras, P. Kim, Atomic and electronic reconstruction at the van der Waals interface in twisted bilayer graphene. *Nat. Mater.* **18**, 448–453 (2019).
15. G. Li, A. Luican, J. M. B. Lopes dos Santos, A. H. Castro Neto, A. Reina, J. Kong, E. Y. Andrei, Observation of van Hove singularities in twisted graphene layers. *Nat. Phys.* **6**, 109–113 (2010).
16. M. Yankowitz, J. Xue, D. Cormode, J. D. Sanchez-Yamagishi, K. Watanabe, T. Taniguchi, P. Jarillo-Herrero, P. Jacquod, B. J. LeRoy, Emergence of superlattice Dirac points in graphene on hexagonal boron nitride. *Nat. Phys.* **8**, 382–386 (2012).
17. A. Kerelsky, L. J. McGilly, D. M. Kennes, L. Xian, M. Yankowitz, S. Chen, K. Watanabe, T. Taniguchi, J. Hone, C. Dean, A. Rubio, A. N. Pasupathy, Maximized electron interactions at the magic angle in twisted bilayer graphene. *Nature* **572**, 95–100 (2019).
18. Y. Choi, J. Kemmer, Y. Peng, A. Thomson, H. Arora, R. Polski, Y. Zhang, H. Ren, J. Alicea, G. Refael, F. von Oppen, K. Watanabe, T. Taniguchi, S. Nadj-Perge, Electronic correlations in twisted bilayer graphene near the magic angle. *Nat. Phys.* **15**, 1174–1180 (2019).
19. Y. Xie, B. Lian, B. Jäck, X. Liu, C.-L. Chiu, K. Watanabe, T. Taniguchi, B. A. Bernevig, A. Yazdani, Spectroscopic signatures of many-body correlations in magic-angle twisted bilayer graphene. *Nature* **572**, 101–105 (2019).
20. Y. Jiang, X. Lai, K. Watanabe, T. Taniguchi, K. Haule, J. Mao, E. Y. Andrei, Charge order and broken rotational symmetry in magic angle twisted bilayer graphene. *Nature* **573**, 91–95 (2019).
21. C. R. Woods, L. Britnell, A. Eckmann, R. S. Ma, J. C. Lu, H. M. Guo, X. Lin, G. L. Yu, Y. Cao, R. V. Gorbachev, A. V. Kretinin, J. Park, L. A. Ponomarenko, M. I. Katsnelson, Y. N. Gornostyrev, K. Watanabe, T. Taniguchi, C. Casiraghi, H.-J. Gao, A. K. Geim, K. S. Novoselov, Commensurate–incommensurate transition in graphene on hexagonal boron nitride. *Nat. Phys.* **10**, 451–456 (2014).
22. P. Gallagher, M. Lee, F. Amet, P. Maksymovych, J. Wang, S. Wang, X. Lu, G. Zhang, K. Watanabe, T. Taniguchi, D. Goldhaber-Gordon, Switchable friction enabled by nanoscale self-assembly on graphene. *Nat. Commun.* **7**, 10745 (2016).
23. S. S. Sunku, G. X. Ni, B. Y. Jiang, H. Yoo, A. Sternbach, A. S. McLeod, T. Stauber, L. Xiong, T. Taniguchi, K. Watanabe, P. Kim, M. M. Fogler, D. N. Basov, Photonic crystals for nano-light in moiré graphene superlattices. *Science* **362**, 1153–1156 (2018).
24. L. J. McGilly, A. Kerelsky, N. R. Finney, K. Shapovalov, E.-M. Shih, A. Ghiotto, Y. Zeng, S. L. Moore, W. Wu, Y. Bai, K. Watanabe, T. Taniguchi, M. Stengel, L. Zhou, J. Hone, X.-Y. Zhu, D. N. Basov, C. Dean, C. E. Dreyer, A. N. Pasupathy, Visualization of moiré superlattices. *Nat. Nanotech.* **15**, 580–584 (2020).
25. Z. Wang, Y. B. Wang, J. Yin, E. Tóvári, Y. Yang, L. Lin, M. Holwill, J. Birkbeck, D. J. Perello, S. Xu, J. Zultak, R. V. Gorbachev, A. V. Kretinin, T. Taniguchi, K. Watanabe, S. V. Morozov, M. Anđelković, S. P. Milovanović, L. Covaci, F. M. Peeters, A. Mishchenko, A. K. Geim,

K. S. Novoselov, V. I. Fal'ko, A. Knothe, C. R. Woods, Composite super-moiré lattices in double-aligned graphene heterostructures. *Sci. Adv.* **5**, eaay8897 (2019).
26. Z. Yu, A. Song, L. Sun, Y. Li, L. Gao, H. Peng, T. Ma, Z. Liu, J. Luo, Understanding interlayer contact conductance in twisted bilayer graphene. *Small* **16**, 1902844 (2020).
27. K. Lai, W. Kundhikanjana, M. A. Kelly, Z.-X. Shen, Nanoscale microwave microscopy using shielded cantilever probes. *Appl. Nanosci.* **1**, 13–18 (2011).
28. L. Gross, F. Mohn, N. Moll, P. Liljeroth, G. Meyer, The chemical structure of a molecule resolved by atomic force microscopy. *Science* **325**, 1110–1114 (2009).
29. J. Zhang, P. Chen, B. Yuan, W. Ji, Z. Cheng, X. Qiu, Real-space identification of intermolecular bonding with atomic force microscopy. *Science* **342**, 611–614 (2013).
30. S. S. Hong, J. J. Cha, Y. Cui, One nanometer resolution electrical probe via atomic metal filament formation. *Nano Lett.* **11**, 231–235 (2011).
31. E. J. H. Soh, S. G. Sarwat, G. Mazzotta, B. F. Porter, M. Riede, R. Nicholas, J. S. Kim, H. Bhaskaran, Filamentary high-resolution electrical probes for nanoengineering. *Nano Lett.* **20**, 1067–1073 (2020).
32. D. A. Scrymgeour, A. Baca, K. Fishgrab, R. J. Simonson, M. Marshall, E. Bussmann, C. Y. Nakakura, M. Anderson, S. Misra, Determining the resolution of scanning microwave impedance microscopy using atomic-precision buried donor structures. *Appl. Surf. Sci.* **423**, 1097–1102 (2017).
33. E. Khestanova, F. Guinea, L. Fumagalli, A. K. Geim, I. V. Grigorieva, Universal shape and pressure inside bubbles appearing in van der waals heterostructures. *Nat. Commun.* **7**, 12587 (2016).
34. C. Tonnoir, A. Kimouche, J. Coraux, L. Magaud, B. Delsol, B. Gilles, C. Chapelier, Induced superconductivity in graphene grown on rhenium. *Phys. Rev. Lett.* **111**, 246805 (2013).
35. J. Lu, L. C. Gomes, R. W. Nunes, A. H. Castro Neto, K. P. Loh, Lattice relaxation at the interface of two-dimensional crystals: Graphene and hexagonal boron-nitride. *Nano Lett.* **14**, 5133–5139 (2014).
36. P. Pochet, B. C. McGuigan, J. Coraux, H. T. Johnson, Toward moiré engineering in 2D materials via dislocation theory. *Appl. Mater. Today* **9**, 240–250 (2017).
37. W. Yang, G. Chen, Z. Shi, C.-C. Liu, L. Zhang, G. Xie, M. Cheng, D. Wang, R. Yang, D. Shi, K. Watanabe, T. Taniguchi, Y. Yao, Y. Zhang, G. Zhang, Epitaxial growth of single-domain graphene on hexagonal boron nitride. *Nat. Mater.* **12**, 792–797 (2013).
38. H. Li, M. I. B. Utama, S. Wang, W. Zhao, S. Zhao, X. Xiao, Y. Jiang, L. Jiang, T. Taniguchi, K. Watanabe, A. Weber-Bargioni, A. Zettl, F. Wang, Global control of stacking-order phase transition by doping and electric field in few-layer graphene. *Nano Lett.* **20**, 3106–3112 (2020).
39. S. Hattendorf, A. Georgi, M. Liebmann, M. Morgenstern, Networks of ABA and ABC stacked graphene on mica observed by scanning tunneling microscopy. *Surf. Sci.* **610**, 53–58 (2013).
40. H. Min, A. H. MacDonald, Electronic structure of multilayer graphene. *Prog. Theor. Phys. Suppl.* **176**, 227–252 (2008).
41. D. Wong, Y. Wang, J. Jung, S. Pezzini, A. M. DaSilva, H.-Z. Tsai, H. S. Jung, R. Khajeh, Y. Kim, J. Lee, S. Kahn, S. Tollabimazraehno, H. Rasool, K. Watanabe, T. Taniguchi, A. Zettl, S. Adam, A. H. MacDonald, M. F. Crommie, Local spectroscopy of moiré-induced electronic structure in gate-tunable twisted bilayer graphene. *Phys. Rev. B* **92**, 155409 (2015).
42. L. Ye, M. Kang, J. Liu, F. von Cube, C. R. Wicker, T. Suzuki, C. Jozwiak, A. Bostwick, E. Rotenberg, D. C. Bell, L. Fu, R. Comin, J. G. Checkelsky, Massive Dirac fermions in a ferromagnetic Kagome metal. *Nature* **555**, 638–642 (2018).
43. T.-H. Han, J. S. Helton, S. Chu, D. G. Nocera, J. A. Rodriguez-Rivera, C. Broholm, Y. S. Lee, Fractionalized excitations in the spin-liquid state of a Kagome-lattice antiferromagnet. *Nature* **492**, 406–410 (2012).
44. J.-X. Yin, S. S. Zhang, G. Chang, Q. Wang, S. S. Tsirkin, Z. Guguchia, B. Lian, H. Zhou, K. Jiang, I. Belopolski, N. Shumiya, D. Multer, M. Litskevich, T. A. Cochran, H. Lin, Z. Wang, T. Neupert, S. Jia, H. Lei, M. Z. Hasan, Negative flat band magnetism in a spin–orbit-coupled correlated Kagome magnet. *Nat. Phys.* **15**, 443–448 (2019).
45. C. K. Thomas, T. H. Barter, T.-H. Leung, M. Okano, G.-B. Jo, J. Guzman, I. Kimchi, A. Vishwanath, D. M. Stamper-Kurn, Mean-field scaling of the superfluid to Mott insulator transition in a 2D optical superlattice. *Phys. Rev. Lett.* **119**, 100402 (2017).
46. T. H. Barter, T.-H. Leung, M. Okano, M. Block, N. Y. Yao, D. M. Stamper-Kurn, Spatial coherence of a strongly interacting Bose gas in the trimerized Kagome lattice. *Phys. Rev. A* **101**, 011601 (2020).
47. Z. Chu, E. C. Regan, X. Ma, D. Wang, Z. Xu, M. I. B. Utama, K. Yumigeta, M. Blei, K. Watanabe, T. Taniguchi, S. Tongay, F. Wang, K. Lai, Nanoscale conductivity imaging of correlated electronic states in WSe_2/WS_2 moiré superlattices. *Phys. Rev. Lett.* **125**, 186803 (2020).
48. X. Huang, T. Wang, S. Miao, C. Wang, Z. Li, Z. Lian, T. Taniguchi, K. Watanabe, S. Okamoto, D. Xiao, S.-F. Shi, Y.-T. Cui, Correlated insulating states at fractional fillings of the WS_2/WSe_2 moiré lattice. Preprint at https://arxiv.org/abs/2007.11155 (2020).
49. K. Kim, M. Yankowitz, B. Fallahazad, S. Kang, H. C. P. Movva, S. Huang, S. Larentis, C. M. Corbet, T. Taniguchi, K. Watanabe, S. K. Banerjee, B. J. LeRoy, E. Tutuc, van der Waals heterostructures with high accuracy rotational alignment. *Nano Lett.* **16**, 1989–1995 (2016).
50. Y. Cao, J. Y. Luo, V. Fatemi, S. Fang, J. D. Sanchez-Yamagishi, K. Watanabe, T. Taniguchi, E. Kaxiras, P. Jarillo-Herrero, Superlattice-induced insulating states and valley-protected orbits in twisted bilayer graphene. *Phys. Rev. Lett.* **117**, 116804 (2016).
51. Y. Yang, K. Lai, Q. Tang, W. Kundhikanjana, M. A. Kelly, K. Zhang, Z.-x. Shen, X. Li, Batch-fabricated cantilever probes with electrical shielding for nanoscale dielectric and conductivity imaging. *J. Micromech. Microeng.* **22**, 115040 (2012).
52. C. Gao, T. Wei, F. Duewer, Y. Lu, X.-D. Xiang, High spatial resolution quantitative microwave impedance microscopy by a scanning tip microwave near-field microscope. *Appl. Phys. Lett.* **71**, 1872–1874 (1997).
53. K. Lai, H. Peng, W. Kundhikanjana, D. T. Schoen, C. Xie, S. Meister, Y. Cui, M. A. Kelly, Z.-X. Shen, Nanoscale electronic inhomogeneity in In_2Se_3 nanoribbons revealed by microwave impedance microscopy. *Nano Lett.* **9**, 1265–1269 (2009).
54. E. Y. Ma, Y.-T. Cui, K. Ueda, S. Tang, K. Chen, N. Tamura, P. M. Wu, J. Fujioka, Y. Tokura, Z.-X. Shen, Mobile metallic domain walls in an all-in-all-out magnetic insulator. *Science* **350**, 538–541 (2015).
55. D. Wu, X. Li, L. Luan, X. Wu, W. Li, M. N. Yogeesh, R. Ghosh, Z. Chu, D. Akinwande, Q. Niu, K. Lai, Uncovering edge states and electrical inhomogeneity in MoS_2 field-effect transistors. *Proc. Natl. Acad. Sci. U.S.A.* **113**, 8583–8588 (2016).
56. Y.-T. Cui, E. Y. Ma, Z.-X. Shen, Quartz tuning fork based microwave impedance microscopy. *Rev. Sci. Instrum.* **87**, 063711 (2016).
57. E. Seabron, S. MacLaren, X. Xie, S. V. Rotkin, J. A. Rogers, W. L. Wilson, Scanning probe microwave reflectivity of aligned single-walled carbon nanotubes: Imaging of electronic structure and quantum behavior at the nanoscale. *ACS Nano* **10**, 360–368 (2016).
58. T. S. Jones, C. R. Pérez, J. J. Santiago-Avilés, Quantitative microwave impedance microscopy with effective medium approximations. *AIP Adv.* **7**, 025207 (2017).
59. S. R. Johnston, E. Y. Ma, Z.-X. Shen, Optically coupled methods for microwave impedance microscopy. *Rev. Sci. Instrum.* **89**, 043703 (2018).
60. S. Plimpton, Fast parallel algorithms for short-range molecular dynamics. *J. Comp. Phys.* **117**, 1–19 (1995).
61. N. Leconte, J. Jung, S. Lebègue, T. Gould, Moiré-pattern interlayer potentials in van der Waals materials in the random-phase approximation. *Phys. Rev. B* **96**, 195431 (2017).
62. M. Wen, S. Carr, S. Fang, E. Kaxiras, E. B. Tadmor, Dihedral-angle-corrected registry-dependent interlayer potential for multilayer graphene structures. *Phys. Rev. B* **98**, 235404 (2018).
63. N. Leconte, S. Javvaji, J. An, J. Jung, Relaxation effects in twisted bilayer graphene: A multi-scale approach. Preprint at https://arxiv.org/abs/1910.12805 (2019).
64. J. Jung, A. H. MacDonald, Accurate tight-binding models for the π bands of bilayer graphene. *Phys. Rev. B* **89**, 035405 (2014).
65. S. Fang, E. Kaxiras, Electronic structure theory of weakly interacting bilayers. *Phys. Rev. B* **93**, 235153 (2016).
66. S. Carr, S. Fang, P. Jarillo-Herrero, E. Kaxiras, Pressure dependence of the magic twist angle in graphene superlattices. *Phys. Rev. B* **98**, 085144 (2018).
67. J. Jung, A. Raoux, Z. Qiao, A. H. MacDonald, *Ab initio* theory of moiré superlattice bands in layered two-dimensional materials. *Phys. Rev. B* **89**, 205414 (2014).
68. N. Leconte, J. Jung, Commensurate and incommensurate double moiré interference in graphene encapsulated by hexagonal boron nitride. *2D Mater.* **7**, 031005 (2019).

Acknowledgments: We are grateful for the technical assistance from R. C. Chintala (PrimeNano Inc.) and the discussion with S. Stonemeyer (UC Berkeley). **Funding:** This work was supported by the Director, Office of Science, Office of Basic Energy Sciences, Materials Sciences and Engineering Division, and Molecular Foundry of the U.S. Department of Energy under contract no. DE-AC02-05-CH11231, primarily within the sp2-Bonded Materials Program (KC2207), which provided for the development of the project concept and uMIM measurements. Additional support was provided by the National Science Foundation, under grant DMR-1807322, which provided for the preliminary AFM topography measurements. The graphene device fabrication is supported as part of the Center for Novel Pathways to Quantum Coherence in Materials, an Energy Frontier Research Center funded by the U.S. Department of Energy, Office of Science, Basic Energy Sciences. K.W. and T.T. acknowledge support from the Elemental Strategy Initiative, conducted by the MEXT, Japan (grant number JPMXP0112101001), JSPS KAKENHI (grant number JP20H00354), and the CREST (JPMJCR15F3), JST. A.S. was supported by the Korean National Research Foundation (grant NRF-2020R1A2C3009142) and by KISTI computational resources (grant KSC-2020-CRE-0072). N.L. acknowledges the Korean National Research Foundation (grant NRF-2018R1C1B6004437), the Korea Research Fellowship Program funded by the Ministry of Science and ICT (KRF-2016H1D3A1023826), as well as the computational resources by KISTI (grant KSC-2018-CHA-0077). J.J. was supported by the Samsung Science and Technology Foundation under project SSTF-BAA1802-06. **Author**

contributions: K.L. and M.I.B.U. conceived the idea of the project, performed measurements, analyzed the data with P.D.A. and A.W.-B., and wrote the manuscript with input from all authors. S.K., B.Y., K.L., and M.I.B.U. fabricated all samples and devices. A.S., N.L., and J.J. calculated the band structures. M.V.P.A. performed TEM. S.W. and G.Z. performed CVD growth of graphene. K.W. and T.T. grew the hBN single crystal. A.Z. and F.W. supervised the project. **Competing interests:** The authors declare that they have no competing interests. **Data and materials availability:** All data needed to evaluate the conclusions in the paper are present in the paper and/or the Supplementary Materials. Additional data related to this paper may be requested from the authors.

Submitted 5 June 2020
Accepted 22 October 2020
Published 9 December 2020
10.1126/sciadv.abd1919

Citation: K. Lee, M. I. B. Utama, S. Kahn, A. Samudrala, N. Leconte, B. Yang, S. Wang, K. Watanabe, T. Taniguchi, M. V. P. Altoé, G. Zhang, A. Weber-Bargioni, M. Crommie, P. D. Ashby, J. Jung, F. Wang, A. Zettl, Ultrahigh-resolution scanning microwave impedance microscopy of moiré lattices and superstructures. *Sci. Adv.* **6**, eabd1919 (2020).